Supplementary Material

Experimental Approach:

All experiments were conducted in a contamination free UHV chamber operating at base pressures of a few 10^{-11} Torr. The silver substrate was interfaced to a cold finger designed from oxygen free high conductivity copper with a 0.2 mm sheet of indium foil to promote thermal conductivity as the entire assembly is cooled to 5.5 ± 0.1 K. These temperatures are reached using a closed-cycle helium compressor (Sumitomo Heavy Industries, RDK-415E). The target can rotate in its horizontal plane by using a doubly differentially pumped rotational feedthrough (Thermoionics Vacuum Products, RNN-600/FA/ MCO) as well as a moveable UHV compatible bellow (McAllister, BLT106). The ices were prepared by depositing gas mixtures of carbon monoxide (CO, Aldrich, 99.99 %; $C^{18}O$, Aldrich, 99 % ^{18}O) premixed in a gas mixing chamber with methane (CH_4, Specialty Gases of America, 99.999 %) or ethane (C_2H_6, Gaspro, 99.999 %), respectively. These mixtures were then introduced into the main chamber at 5×10^{-8} Torr through a glass capillary array positioned 30 mm in front of the silver mirror. The deposition was monitored using laser interferometry and the ice thickness was determined *in situ* to be 500 ± 10 nm with a helium-neon (HeNe) laser (CVI Melles-Griot; 25-LHP-230) operating at 632.8 nm; using an index of refraction of the mixed CO – CH_4 ice of 1.31 ± 0.02 and 1.30 ± 0.02 for the $C^{18}O$ – C_2H_6 ice derived from numerical fitting of the intensity ratios (56). Using a modified Lambert-Beer relationship with absorption coefficients of 1.1×10^{-17} cm molecule^{-1}, 3.5×10^{-19} cm molecule^{-1}, 1.6×10^{-19} cm molecule^{-1} and 2.2×10^{-17} cm molecule^{-1} for the 2090 cm^{-1} (ν_1, ^{13}CO) (57), 4204 cm^{-1} ($\nu_1 + \nu_4$, CH_4) (33), 4147 cm^{-1} ($2\nu_1$, $C^{18}O$) (33) and 2973 cm^{-1} (ν_{10}, C_2H_6) (58) bands (Table S1), respectively, a total ice thickness of 500 ± 100 nm (CO – CH_4; 1.0 ± 0.3 : 1.6 ± 0.5) and 450 ± 100 nm ($C^{18}O$ – C_2H_6; 1.0 ± 0.4 : 1.5 ± 0.6) was determined, which is in agreement with the data derived from the laser interferometry method.

Each ice was irradiated with 5 keV electrons for 60 minutes at a current of 30 nA over the 1.0 ± 0.1 cm^2 area at an angle of incidence of 70º with respect to the surface normal of the silver mirror substrate. The average penetration depth of the 5 keV electrons was calculated utilizing Monte Carlo simulations (CASINO) (59) to be 350 ± 40 nm (CO – CH_4) and 320 ± 30 nm ($C^{18}O$ – C_2H_6), which is less than the thickness of the deposited ice mixtures of 500 ± 10 nm ensuring that there is no interaction between the substrate and the electrons. The ice was exposed to doses

of 3.1 ± 1.0 eV per CO molecule and 3.5 ± 1.0 eV per CH_4 molecule for the CO – CH_4 ice mixture and 3.7 ± 1.0 eV per $C^{18}O$ molecule and 5.3 ± 1.3 eV per C_2H_6 molecule. These doses are calculated utilizing the densities of 1.03 g cm^{-3} (60), 0.47 g cm^{-3} (61) and 0.719 g cm^{-3} (62) for carbon monoxide, methane, and ethane, respectively. The ice mixtures were monitored both *online* and *in situ* before, during, and after the irradiation phase of the experiment via a Fourier Transform Infrared (FTIR) spectrometer (Nicolet 6700) in the range of 6,000 to 500 cm^{-1} with a resolution of 4 cm^{-1} in intervals of 2 minutes. This results in the collection of 30 FTIR spectra during the 1 hour irradiation period at 5.5 K. After the irradiation, the ice is held isothermal for an hour, and then temperature programmed desorption (TPD) was exploited to sublime the ice as well as any newly formed products, which can then be detected in the gas phase by heating the substrate to 300 K at 0.5 K min^{-1}.

Abplanalp et al. (2015) (63) provides a detailed account of the PI-ReTOF-MS technique used in this work. Using a reflectron time-of-flight mass spectrometer (Jordan TOF Products, Inc.) coupled with soft photoionization allows the detection of subliming molecules upon photoionization of the neutral molecules. The subliming molecules were analyzed via single photon ionization by using coherent vacuum ultraviolet (VUV) light pulsed at 30 Hz. The VUV generation chamber is operated at a pressure of about 4×10^{-4} Torr, where the backing pressure for the pulse valve is 1,900 Torr. The 10.49 eV photons were produced from the third harmonic of a Nd:YAG laser (354.6 nm; Spectra Physics, PRO-250-30; 333 mJ $pulse^{-1}$) by frequency tripling in pulsed jets of xenon. The xenon gas acts as a non-linear medium in order to produce 118.2 nm (10.49 eV) VUV used to photoionized the subliming molecules. To produce VUV energies of 9.80, 9.60, and 8.40 eV, resonant four-wave difference mixing was utilized ($\omega_{VUV} = 2\omega_1 - \omega_2$). For instance, to produce the 9.60 eV (129.1 nm; ω_{VUV}) photons ultraviolet (202.3 nm; 6.13 eV; ω_1) and visible (466.7 nm; 2.66 eV; ω_2) light was generated by a pair of Nd:YAG pumped dye lasers. The ω_1 light was produced by frequency tripling the dye laser output (Sirah, Cobra-Stretch; 606.9 nm, 2.04 eV) using β-BaB_2O_4 (BBO) crystals (44° and 77°) to generate 202.3 nm (6.13 eV). Similarly, ω_2 light was the output from the second Nd:YAG pumped dye laser (Sirah, Precision Scan) of 466.7 nm (2.66 eV). Once ω_1 and ω_2 were generated the laser beams were then overlapped in time by utilizing a pulse delay generator and spatially through a system of dichroic mirrors that were sensitive to the wavelength needed and then focused through a MgF_2 window (Kurt J. Lesker Company; VPZL-275 UM) using a fused silica bi-

convex lens (Thorlabs LB4265; f =150 mm) into the differentially pumped vacuum chamber that contained the pulsed piezoelectric valve. In this case the non-linear medium consisted of pulsed jets of krypton (99.999 %; Specialty Gases) operated with a backing pressure of 1,520 Torr, at a rate of 30 Hz, and a pulse of 80 μs, which generated the 9.60 eV VUV photons via four-wave difference mixing ($\omega_{VUV} = 2\omega_1 - \omega_2$) (64). However, it should be noted that this process results in the generation of ultraviolet light (ω_1), visible light (ω_2), and VUV light ($2\omega_1 + \omega_2$; $2\omega_1 - \omega_2$; $3\omega_1$; $3\omega_2$), all of which are capable of photoionizing the subliming molecules in theory. This was accounted for by spatially separating the overlapping wavelengths with an off axis lithium fluoride (LiF) planoconvex lens (ISP Optics, LF-PX-38-150; f = 150 mm) (65), which has specific refractive indices for individual wavelengths. Hence only the desired wavelength photo ionizes the subliming molecules. Here, the wavelength of interest was then passed through a 1 mm aperture and then photoionized the subliming molecules 1 mm above the substrate surface. The ions were then analyzed within the reflectron time-of-flight mass spectrometer and detected by a multichannel plate operating in a dual chevron configuration based upon the arrival time. The multichannel plate signals were then amplified (Ortec 9305) and shaped. The corresponding time-of-flight signal was then recorded via a personal computer multichannel scalar (FAST ComTec, P7888-1 E) that operated at 30 Hz (Quantum Composers, 9518) with a 4 ns bin width and 3600 sweeps for each mass spectrum, thus correlating with a change in temperature of 1 K per spectrum during the TPD process. This approach was crucial for discriminating which isomers were formed in the irradiation experiments of both the CO – CH_4 and $C^{18}O$ – C_2H_6 systems.

The complete data sets are compiled in Figure 2 with signal observed up to mass-to-charge ratios (m/z) of m/z = 118 and m/z = 122 for the CO – CH_4 and $C^{18}O$ – C_2H_6 systems, respectively. Accounting for the isotopic substitution pattern, this finding suggests that besides acetaldehyde – vinyl alcohol and propanal – propenol, aldehydes/enols up to $C_6H_{13}HCO$ are synthesized. Previous studies of irradiated methane (CH_4) and D4-methane (CD_4) ices revealed that hydrocarbons up to $C_{22}H_{46}$ are formed (66). Considering the formation pathways of acetaldehyde and propanal via hydrogen loss from the methane and ethane alkane via radiolysis followed by hydrogen atom (H) – carbon monoxide reaction to the formyl radical (HCO) and recombination of the latter with the alkyl radical, COMs up to $C_6H_{13}HCO$ as found in the CO – CH_4 and CO – C_2H_6 systems are likely formed via a similar reaction sequence of a radiolytic

hydrogen loss from the alkane forming the alkyl radical (R), followed by formyl radical formation (HCO), and recombination of the latter with the alkyl radical to the aldehyde (RHCO). The identification of these aldehydes along with their isomers is subject of a forthcoming publication and requires a detailed analysis of the isotopically labeled systems together with the data recorded at different photoionization energies of 10.49 eV, 9.80 eV, 9.60 eV, and 8.40 eV.

The development of infrared band for the formyl radical, methyl radical, acetaldehyde, and vinyl alcohol for the CO – CH_4 system, as well as the formyl radical, ethyl radical, propanal, and (E)/(Z)-1-propenol for the $C^{18}O$ – C_2H_6 ices during the irradiation exposure was continuously monitored (Figs. S2-S3). The formyl, methyl, and ethyl radicals could be fit using pseudo-first-order kinetics (equations (13)-(15))

(S1) $$[HCO](t) = a(1 - e^{-k_1 t}),$$

(S2) $$[CH_3](t) = b(1 - e^{-k_2 t}),$$

(S3) $$[C_2H_5](t) = b'(1 - e^{-k_{2'} t}).$$

Using equations (S1)-(S2) to fit the formyl radical and methyl radical for the CO – CH_4 experimental data determines k_1 = (2.5 ± 0.1) × 10^{-3} s^{-1} and a = (3.8 ± 0.1) × 10^{15} molecules cm^{-2} along with k_2 = (1.5 ± 0.3) × 10^{-3} s^{-1} and b = (1.2 ± 0.1) × 10^{15} molecules cm^{-2}, respectively. Similarly by using equations (S1 and S3) to fit the formyl radical and ethyl radical for the $C^{18}O$ – C_2H_6 experimental data determines k_1 = (2.9 ± 0.1) × 10^{-3} s^{-1} and a = (1.8 ± 0.1) × 10^{15} molecules cm^{-2} and $k_{2'}$ = (1.8 ± 0.4) × 10^{-3} s^{-1} and b′ = (3.6 ± 0.3) × 10^{15} molecules cm^{-2}, respectively.

The production of the keto-enol isomers can be described as the consecutive reaction of (A→B→C), where A corresponds to the reactants, such as a complex or the carbon monoxide and the methane molecule as discussed above, that can form the respective aldehyde (B) via rapid radical reaction of the formyl radical with the methyl radical, which then forms the enol isomers (C). In order to fit the development of acetaldehyde and vinyl alcohol we used these consecutive kinetics (reactions (S4)-(S5)),

(S4) $$[CH_3CHO](t) = \frac{k_3 c}{k_4 - k_3}(e^{-k_3 t} - e^{-k_4 t}),$$

(S5) $$[C_2H_3OH](t) = c\left(1 - \frac{k_4}{k_4 - k_3}e^{-k_3 t} + \frac{k_3}{k_4 - k_3}e^{-k_4 t}\right).$$

In these equations the c term corresponds to the initial concentration of complex A, k_3 defines the

rate of conversion of A to B, and k_4 corresponds to the conversion of B to C. The best fits for the acetaldehyde and vinyl alcohol production were calculated using $k_3 = (4.5 \pm 0.4) \times 10^{-4}$ s^{-1}, $k_4 = (2.7 \pm 0.8) \times 10^{-5}$ s^{-1}, and c = $(1.3 \pm 0.1) \times 10^{15}$ molecules cm^{-2}. Utilizing the corrected infrared column densities assigned to acetaldehyde and vinyl alcohol of 19 %, and 9 %, respectively, and the average energy deposited by the electrons into the ice the yield for each molecule per electron volt absorbed energy can be calculated. This resulted in values of $(4.9 \pm 1.9) \times 10^{-5}$ molecules eV^{-1} and $(4.1 \pm 0.9) \times 10^{-7}$ molecules eV^{-1} for acetaldehyde and vinyl alcohol, respectively.

Theoretical Approach:

Table S2 reports the computed photoionization cross sections of acetaldehyde, vinyl alcohol, propanal, and (E)/(Z)-1-propenol (43). First, geometries were optimized with the ωB97X-D density functional and the aug-cc-pVTZ basis set (44). The Dyson orbitals and ionization energies were then computed in Q-Chem (45) with the coupled-cluster approach using both single and double excitation (CCSD) for the ground-state (S_0) wave function, and equation-of-motion ionization potential CCSD (EOM-IP-CCSD) for the ionized state (D_1) wave function (46-48). The CCSD/EOM-IP-CCSD Dyson orbital calculations utilized the aug-cc-pVTZ basis set. Photoionization cross sections are computed in ezDyson v. 3.0 (43, 46, 49). Ionization energies were computed by taking the difference between the CCSD S_0 energy and the EOM-IP-CCSD D_1 energy, each computed at the respective equilibrium structure to account for geometry relaxation of the ionized state, also accounting for ZPE corrections to the ionization energies at the ωB97X-D/aug-cc-pVTZ level of theory. The FCFs were computed within the double-harmonic and parallel mode approximations using ezSpectrum (50) using S_0 and D_1 structures and frequencies computed with ωB97X-D/aug-cc-pVTZ (*Table S4*). The cross-section calculations also requires the photoelectron wave function which is described by Coulomb waves with a partial (effective) charge Z that is between 0 and 1 (43). Note that when Z = 0 for a Coulomb wave, it becomes exactly a plane wave. The algorithm for predicting this effective charge from first principles is not yet implemented, and so in the present work we resort to computing photoionization cross sections using Coulomb waves with different values of Z ranging from 0 to 1 and testing the sensitivity of branching ratios to the value of Z.

In Table S2, we report the photoionization cross sections for acetaldehyde, vinyl alcohol, propanal, and the two isomers of 1-propenol for different values of the effective charge (Z). Experimental literature values are shown in Table S2; these are only known for acetaldehyde, vinyl alcohol, and propanal. We find that Z = 0, Z = 1, and Z = 0.8 give the best agreement with experimental values for acetaldehyde, vinyl alcohol, and propanal, respectively, but that the cross section does vary considerably with Z. This suggests that there is no clear indication for which Z value should be used to compare the cross sections for the branching ratios. However, at least one value of Z exists for which the computed cross sections are in good agreement with the experimental value for each molecule, and within the reported experimental error of 20-25% (67, 68). This has also been demonstrated for a number of small organic molecules in a recent study (43). Therefore, the branching ratios can then be obtained by using relative cross sections of each aldehyde and corresponding enol at six values of Z (0, 0.2, 0.4, 0.6, 0.8, 1.0) and taking their average. This yields branching ratios that are based on theoretically computed cross sections ("Theoretical Ratios" in Table S3). If instead we use experimentally determined cross sections for acetaldehyde, vinyl alcohol, and propanal and theoretical cross sections just for (E)/(Z)-1-propenol, we obtain the values shown as "Experimental Ratios" in Table S3. We also consider that the "ideal" Z that produces the correct cross section for each system may be different for each aldehyde and its corresponding enol. Therefore, we compute the branching ratios using the combination of Z values for each aldehyde/enol pair that gives the largest and smallest branching ratios, thus giving the range of branching ratios where we can expect with high confidence the true branching ratio to fall. This gives 1.27 : 1 − 3.72 : 1 for acetaldehyde : vinyl alcohol, 1.71 : 1 – 12.46 : 1 for propanal:(E)-1-propenol, and 2.95 : 1 − 16.61 : 1 for propanal:(Z)-1-propenol. Despite the uncertainty in the exact branching ratios of the aldehyde/enol pairs, the analysis above clearly suggests that the experimentally derived branching ratios are several orders of magnitude larger than those expected from thermal processes.

Determination of Keto – Enol Branching Ratios:

In the experiments exploiting a photoionization energy of 10.49 eV, the TPD profile portraying the ion currents of m/z = 44 (CO-CH_4) and 60 ($C^{18}O$ – C_2H_6) versus the temperature, hereafter $TPD_{44}(T)$ and $TPD_{60}(T)$, represent a linear combination of the individual TPD profiles of the aldehydes ($TPD_{44(aldehyde)}(T)$ and $TPD_{60(aldehyde)}(T)$) and the enols ($TPD_{44(enol)}(T)$ and

$TPD_{60(enol)}(T)$) (Fig S5A) (S6 and S7).

(S6) $TPD_{44}(T) = TPD_{44(aldehyde)}(T) + f_1 \times TPD_{44(enol)}(T) = TPD_{44(aldehyde)}(T) + TPD'_{44(enol)}(T)$

(S7) $TPD_{60}(T) = TPD_{60(aldehyde)}(T) + f_2 \times TPD_{60(enol)}(T) = TPD_{60(aldehyde)}(T) + TPD'_{60(enol)}(T)$

The tunable experiments below 10.49 eV resulted in signal belonging only to the TPD profile of the enol isomers, $TPD_{44(enol)}(T)$ and $TPD_{60(enol)}(T)$; considering that the ion intensity depends on the photoionization wavelength due to distinct photoionization cross sections, this signal was scaled with scaling factors f_1 and f_2 to the intensity that was detected in the 10.49 eV experiment (Fig. S5B). Next, the signal belonging to the enol isomer ($f_1 \times TPD_{44(enol)}(T) = TPD'_{44(enol)}(T)$ and $f_2 \times TPD_{60(enol)}(T) = TPD'_{60(enol)}(T)$) was subtracted from the signal at 10.49 eV ($TPD_{44}(T)$ and $TPD_{60}(T)$). This remaining signal after subtraction corresponds to the TPD profile of the aldehyde isomer ($TPD_{44(aldehyde)}(T)$ and $TPD_{60(aldehyde)}(T)$) (Fig. S5C-red). Therefore, the TPD profiles recorded at 10.49 eV can be effectively decoupled into individual contributions from the aldehydes ($TPD_{44(aldehyde)}(T)$ and $TPD_{60(aldehyde)}(T)$) and the enols ($TPD'_{44(enol)}(T)$ and $TPD'_{60(enol)}(T)$). Finally, since each isomer at 10.49 eV has a different photoionization cross-section, the integrated individual TPD profiles had to be normalized using their respective photoionization cross-sections at 10.49 eV (Fig. S5D) prior to integration. Table S2 compiles the experimentally determined photoionization cross sections as available from literature as well as computed photoionization cross sections for the keto-enol isomers detected in these experiments by varying the effective charge (Z) from 0.0 – 1.0 (*Theoretical Approach*). The photoionization cross sections were then applied to each respective isomer integrated ion signal as a normalization factor (Fig. S5D). Therefore, the ratios of the integrated normalized signals are equivalent to the aldehyde to enol relative ratio (Table S3).

The determination of these branching ratios provides specific details on the conditions of their synthesis. If the tautomers are synthesized within a thermodynamical equilibrium process during the warm up in the gas-phase, keto-enol branching ratios of 3.80×10^{249} (10 K) to 1.94×10^{11} (200 K) for acetaldehyde versus vinyl alcohol, 6.34×10^{88} (10 K) and 2.75×10^{4} (200 K) for propanal versus (E)-1-propenol, and 4.8×10^{62} (10 K) along with 1.4×10^{3} (200 K) for propanal versus (Z)-1-propenol are expected. A comparison of the thermodynamically predicted ratios with the experimentally derived branching ratios of 2.68 ± 1.02 (acetaldehyde : vinyl alcohol), 3.20 ± 0.80 (propanal : (E)-1-propenol), and 4.23 ± 0.96 (propanal : (Z)-1-propenol) shows an

overproduction of the enols.

These branching ratios provide valuable information on the conditions during their synthesis. If the tautomers are synthesized within a thermodynamical equilibrium process during the warm up in the gas-phase, i.e. a hypothetical tautomerization of the subliming acetaldehyde to the vinyl alcohol, this route is connected with an equilibrium constant K defined as the quotient of the concentration of the keto and enol tautomers with K = [keto]/[enol] = exp (-ΔG/RT) at the temperature T with R being the ideal gas constant and ΔG the difference in standard Gibbs free energies of the keto and enol tautomers: ΔG (acetaldehyde - vinyl alcohol) = - 43 kJ mol^{-1}, ΔG (propanal : (E)-1-propenol) = -17 kJ mol^{-1}, and ΔG (propanal : (Z)-1-propenol) = -12 kJ mol^{-1}. Hence, within the temperature range from 10 K to 200 K with the latter defining the maximum temperature at which the keto and enol forms have sublimed, keto-enol branching ratios of 3.80 × 10^{249} (10 K) and of 1.94 × 10^{11} (200 K) for acetaldehyde versus vinyl alcohol, 6.34 × 10^{88} (10 K) along with 2.75 × 10^{4} (200 K) for propanal versus (E)-1-propenol and 4.8 × 10^{62} (10 K) and 1.4 × 10^{3} (200 K) for propanal versus (Z)-1-propenol are expected. Therefore, we should detect fractions of the enol tautomers at levels of 6 ppt, 36 ppm, and 734 ppm, for vinyl alcohol, (E)-1-propenol, and (Z)-1-propenol, respectively, if they are formed via thermal reactions. However, a comparison of these data with the experimentally derived branching ratios of 2.68 ± 1.02 (acetaldehyde : vinyl alcohol), 3.20 ± 0.80 (propanal : (E)-1-propenol), and 4.23 ± 0.96 (propanal : (Z)-1-propenol) exposes a significant *overproduction* of the enol tautomers by 249, 88, and 62 orders of magnitude, respectively. Therefore, our data reveal that in our experiments, these tautomers are not formed under thermal equilibrium conditions within the warm up phase of the ices, but through non-equilibrium processes at ultralow temperatures.

Astrochemical Modeling. In the present work, astrochemical networks were used to explore the impact of the non-equilibrium chemistry on the production of these complex molecules (*Tables S5-S7*). These models consisted of average conditions in SgrB2(N) (T_{gas} = 50 K; T_{grain} = 15 K) and were first run for each environment with a cosmic-ray ionization rate of $\zeta = 10^{-16}$ s^{-1}, as supported by recent observations by the Atacama Pathfinder Experiment (APEX) and the addition of vinyl alcohol to the gas-grain network (*Table S6*). Then, the models were simulated again including the reactions in the network given by reactions (3)-(7), i.e. the novel chemistry described in this work within the icy grains (*Table S7*). To model the astrochemical process that

involves reactions within the ice, the actually observed abundances of the constituents of the ice must be taken into consideration. In interstellar grain ice mantles, carbon monoxide is typically more abundant than methane, thus, the rate limiting step used in these models is the formation of the energetic hydrogen atom from the dissociation of methane, given by reaction (4). The rate coefficient, $JCH_4(s^{-1})$, for this process was calculated using the formula (13) $JCH_4 = S_e G_{tot} \varphi$ where φ is the radiation flux, S_e is the electronic stopping cross-section of the electrons in the medium being considered, and G_{tot} is the total geminacy factor, i.e. the number of species produced per eV of energy deposited by the incoming particle summed over all product channels (54). From the experimental data, G_{tot} was determined to have a value of 12.2 ± 1.3 molecules eV^{-1}. This value can be considered to be a first-order approximation of the efficiency of the radiation chemistry of carbon monoxide and methane. However, the case of real interstellar grains would have carbon monoxide and methane adsorbed in an amorphous solid water (ASW) matrix (55). This dilution effect of being in the ASW matrix is accounted for the model in terms of the abundances used in calculating the total rates, as well as in the electronic stopping cross-section, S_e, used in determining the rate coefficient. The calculated value of the electronic stopping cross-section was $S_e = 2.8 \times 10^{-18}$ eV cm^2 $molecule^{-1}$ as derived using ESTAR (51), which utilizes the density-corrected formulation of the Bethe equation (52, 53). Using a standard cosmic-ray flux of $\varphi \approx 10$ cm^{-2} s^{-1} thus results in a rate-coefficient of $JCH_4 \approx (3.42 \pm 0.35) \times 10^{-16}$ s^{-1}. Given the complexity of the physical processes involved in the chemistry of irradiated solids, this rate coefficient should be seen as an overall value that includes the contributions of secondary electrons and recoils. Also, the models calculate rate coefficients for diffusive grain-surface reactions using the diffusion energy barrier, E_d. Considering a kinetic energy of the hydrogen atoms of a few eV, the models incorporate the suprathermal hydrogen formed via reaction (4) as being able to diffuse barrierlessly. Meanwhile the formyl radical (HCO) formed via reaction (5) was calculated as having a reduced diffusion barrier of 537 K utilizing the standard diffusion formula $k_{diff} = \nu \exp(-E_d/T)$ and k_4 determined from the experimental results. In the standard diffusion formula E_d is the diffusive barrier, ν is some trial frequency for physisorbed species, here given a customary value of 1×10^{12} s^{-1}, and T is the ice temperature. In order to incorporate the laboratory measurement of the rate coefficient for reaction (6) into the interstellar models as a function of temperature, we treated the reaction as a diffusive one with a first-order rate coefficient for hopping from one potential well to an adjacent one. It is important

to clarify that accounting for Spitzer data, the ice composition can vary with the source (low- and high-mass protostars, background stars) as demonstrated for instance for carbon monoxide (CO), whose abundances can vary from 3 to 50 %, often within the presence of water (polar ices). Therefore, it is not feasible to define a unique model ice in laboratory simulation experiments, but it is important to approximate ices as 'typical' model ices. Second, real interstellar grains are not only exposed to a range of energetic GCRs but also to ultraviolet photons; the latter only interact with the first few icy layers of the grains, whereas energetic GCRs can penetrate the icy mantle; therefore, GCR and ultraviolet exposure can lead to different keto – enol branching ratios, but the astronomical surveys observe the results of cumulative effects of GCRs and photon exposure of interstellar ices. It should be noted that the observed abundances of selected COMs such as ethers (dimethylether) in hot cores and hot corinos can be reproduced by astrochemical models, but these are special cases and do not involve a versatile route to reproduce the overall abundances of COMs (69).

References

56. Goodman AM (1978) Optical interference method for the approximate determination of refractive index and thickness of a transparent layer. *Appl Opt* 17(17):2779-2787.
57. Garozzo M, Fulvio D, Kanuchova Z, Palumbo ME, & Strazzulla G (2010) The fate of s-bearing species after ion irradiation of interstellar icy grain mantles. *Astron Astrophys* 509(A67):1-9.
58. Hudson R, Gerakines P, & Moore M (2014) Infrared spectra and optical constants of astronomical ices: II. Ethane and ethylene. *Icarus* 243:148-157.
59. Drouin D, *et al.* (2007) Casino v2.42—a fast and easy-to-use modeling tool for scanning electron microscopy and microanalysis users. *Scanning* 29(3):92-101.
60. Jiang GJ, Person WB, & Brown KG (1975) Absolute infrared intensities and band shapes in pure solid co and co in some solid matrices. *J Chem Phys* 62(4):1201-1211.
61. Satorre MÁ, *et al.* (2008) Density of CH_4, N_2, and CO_2 ices at different temperatures of deposition. *Planet Space Sci* 56(10):1748-1752.
62. van Nes GJH (1978) Single-crystal structures and electron density distributions of ethane, ethylene and acetylene. PhD thesis (University of Groningen).
63. Abplanalp MJ, Borsuk A, Jones BM, & Kaiser RI (2015) On the formation and isomer specific detection of propenal (C_2H_3CHO) and cyclopropanone (c-C_3H_4O) in interstellar model ices—a combined ftir and reflectron time-of-flight mass spectroscopic study. *Astrophys J* 814(1):45-61.
64. Hilbig R & Wallenstein R (1982) Narrowband tunable vuv radiation generated by nonresonant sum- and difference-frequency mixing in xenon and krypton. *Appl Opt* 21(5):913-917.
65. VonDrasek WA, Okajima S, & Hessler JP (1988) Efficient monochromator to isolate vuv light generated by four-wave mixing techniques. *Appl Opt* 27(19):4057-4061.
66. Jones BM & Kaiser RI (2013) Application of reflectron time-of-flight mass spectroscopy in the analysis of astrophysically relevant ices exposed to ionization radiation: methane (CH_4) and D4-methane (CD_4) as a case study. *J Phys Chem Lett* 4(11):1965-1971.
67. Cool TA, *et al.* (2003) Selective detection of isomers with photoionization mass spectrometry for studies of hydrocarbon flame chemistry. *J Chem Phys* 119(16):8356-8365.
68. Wang J, Yang B, Cool TA, Hansen N, & Kasper T (2008) Near-threshold absolute photoionization cross-sections of some reaction intermediates in combustion. *Int J Mass Spec* 269(3):210-220.
69. Taquet V, Wirström E, & Charnley SB (2016) Formation and recondensation of complex organic molecules during protostellar luminosity outbursts. *Astrophys J* (accepted for publication):1-12.
70. Bennett CJ, Jamieson CS, Osumura Y, & Kaiser RI (2006) Laboratory studies on the irradiation of methane in interstellar, cometary, and solar system ices. *Astrophys J* 653(1):792-811.
71. Jamieson CS, Mebel AM, & Kaiser RI (2006) Understanding the kinetics and dynamics of radiation-induced reaction pathways in carbon monoxide ice at 10 k. *Astrophy J Suppl Ser* 163(1):184-206.
72. Hepp M & Herman M (1999) Weak combination bands in the 3-μm region of ethane. *J Mol Spectrosc* 197(1):56-63.
73. Kanno N & Tonokura K (2007) Vacuum ultraviolet photoionization mass spectra and

crosssections for volatile organic compounds at 10.5 ev. *Appl Spectrosc* 61(8):896-902.
74. Turner BE & Apponi AJ (2001) Microwave detection of interstellar vinyl alcohol, CH_2CHOH. *Astrophys J Lett* 561(2):L207-L210.

Table S1a. Infrared absorption features recorded before and after the irradiation of carbon monoxide-methane ices (CO - CH_4) at 5.5 K.

CH_4:CO				
Before Irradiation (cm^{-1})	After Irradiation (cm^{-1})	assignment	carrier	ref.
4534, 4302, 4204		$\nu_2+\nu_3$, $\nu_3+\nu_4$, $\nu_1+\nu_4$ (CH_4)	Combinations	(70)
4248		$2\nu_1$ (CO)	Overtone	(71)
	3253	ν_3 (C_2H_2)	CH stretch	(70)
	3239	ν_2 (C_2H_3OH)	CH_2 asymmetric stretch	(30)
	3093	ν_9 (C_2H_4)	CH_2 asymmetric stretch	(70)
3011		ν_3 (CH_4)	degenerate stretch	(70)
	2978	ν_{10} (C_2H_6)	CH_3 degenerate stretch	(70)
	2962	ν_1 (C_2H_6)	CH_3 symmetric stretch	(70)
	2943	$\nu_8+\nu_{11}$ (C_2H_6)	Combination	(70)
	2920	$\nu_8+\nu_{11}$ (C_2H_6)	Combination	(70)
2905		ν_1 (CH_4)	CH symmetric stretch	(70)
	2885	ν_5 (C_2H_6)	CH_3 symmetric stretch	(70)
2818		$\nu_2+\nu_4$ (CH_4)	Combination	(70)
	2748	$\nu_2+\nu_6$ (C_2H_6)	Combination	(70)
2595		$2\nu_4$ (CH_4)	Overtone	(70)
	2341	ν_3 (CO_2)	CO asymmetric stretch	(71)
	2276	ν_3 ($^{13}CO_2$)	CO asymmetric stretch	(71)
	2242	ν_3 (C_3O_2)	CO asymmetric stretch	(71)
	2192	ν_1 (C_3O_2)	CO stretch	(71)
2137		ν_1 (CO)	CO stretch	(71)
2090		ν_1 (^{13}CO)	CO stretch	(71)
	1853	ν_3 (HCO)	CO stretch	(16)
	1790-1600	a	CO stretch	(33)
	1646	ν_4 (C_4H_8)	C=C stretch	(34)
	1635	ν_5 (C_2H_3OH)	C=C stretch	(30)
	1466	ν_{11} (C_2H_6)	CH_3 deformation	(70)
	1427	ν_{12} (CH_3CHO)	CH_3 deformation	(16)
	1373	ν_6 (C_2H_6)	CH_3 symmetric deformation	(70)
	1350	ν_7 (CH_3CHO)	CH_3 deformation	(16)
1302		ν_4 (CH_4)	Degenerate stretch	(70)
	1130	ν_9 (C_2H_3OH)	CO stretch	(30)
	1120	ν_8 (CH_3CHO)	CH_3 deformation	(16)
	1091	ν_2 (HCO)	Bending	(16)
	957	ν_7 (C_2H_4)	CH_2 wag	(34)
	821	ν_{12} (C_2H_6)	Bending	(34)
	613	ν_2 (CH_3)	Out of plane	(70)

Notes: (a) Carbonyl stretching region (saturated/unsaturated aldehydes/ketones with mono-/di-/tri-/tetra- substituted side chains)

Table S1b. Infrared absorption features recorded before and after the irradiation of O^{18}-carbon monoxide-ethane - ices ($C^{18}O$ - C_2H_6) at 5.5 K

$C^{18}O:C_2H_6$				
Before Irradiation (cm^{-1})	After Irradiation (cm^{-1})	Assignment	Carrier	References
4400, 4356, 4322, 4271, 4250, 4186, 4160, 4125, 4084, 4068		$\nu_8+\nu_{10}$, $\nu_2+\nu_7$, $\nu_6+\nu_{10}$, $\nu_1+\nu_6$, $\nu_2+\nu_5$, $\nu_7+\nu_{12}$, $\nu_7+\nu_{12}$, $\nu_8+\nu_{11}+\nu_{12}$, $\nu_8+\nu_{11}+\nu_{12}$, $\nu_5+\nu_{12}$ (C_2H_6)	Overtones/ Combinations	(34)
4147		$2\nu_1$ ($C^{18}O$)	Overtone	(33)
3258		$\nu_4+\nu_7$ (C_2H_6)	Combination	(72)
	3105	ν_{10} (C_2H_5)	CH_2 asymmetric stretch	(34)
	3091	ν_9 (C_2H_4)	CH_2 asymmetric stretch	(33)
	3008	ν_3 (CH_4)	Deg. stretch	(33)
2973		ν_{10} (C_2H_6)	CH_3 stretch	(33)
2959		ν_1 (C_2H_6)	CH_3 stretch	(33, 70)
2942		$\nu_8+\nu_{11}$ (C_2H_6)	Combination	(72)
2913		$\nu_8+\nu_{11}$ (C_2H_6)	Combination	(72)
2881		ν_5 (C_2H_6)	CH_3 symmetric stretch	(33)
2852		$\nu_2+\nu_4+\nu_{12}$ (C_2H_6)	Combination	(72)
2827		$\nu_6+\nu_{11}$ (C_2H_6)	Combination	(72)
2739		$\nu_2+\nu_6$ (C_2H_6)	Combination	(33)
2648		$\nu_8+\nu_{12}$ (C_2H_6)	Combination	(72)
2558		$\nu_6+\nu_9$ (C_2H_6)	Combination	(33)
2359		$\nu_3+\nu_6$ (C_2H_6)	Combination	(72)
	2338	ν_3 (^{18}OCO)	CO asymmetric stretch	(71)
	2323	ν_3 (CO_2)	CO asymmetric stretch	(33)
	2310	ν_3 ($C^{18}O_2$)	CO asymmetric stretch	(71)
	2227	ν_3 ($C_3{}^{18}O_2$)	CO asymmetric stretch	(71)
	2161	ν_1 ($C_3{}^{18}O_2$)	CO stretch	(71)
2136		ν_1 (CO)	CO stretch	(33)
2110		ν_1 (CO-Ag)	CO stretch	(71)
2089		ν_1 ($C^{18}O$)	CO stretch	(33)
	1811	ν_3 $HC^{18}O$	CO stretch	(33)
	1740-1600	a	CO stretch	(33)
	1645	ν_4 (C_4H_8)	C=C stretch	(23)
1463		ν_{11} (C_2H_6)	CH_3 deformation	(23)
	1435	ν_{12} (C_2H_4)/ ν_s ($C_2H_5O^{18}H$)	CH_2 scissor/ CH stretch	(32, 33)
1371		ν_6 (C_2H_6)	CH_3 deformation	(33)
	1340	ν_9 ($C_2H_5O^{18}H$)	CH_2 wag	(32)
	1301	ν_4 (CH_4)	Degenerate stretch	(33)
	1083	ν_2 $HC^{18}O$	CO stretch	(33)
	974	ν_{35} (C_4H_{10})	CH_3 rock	(34)
	951	ν_7 (C_2H_4)	CH_2 wag	(34)
820		ν_{12} (C_2H_6)	Bending	(34)
	758	ν_5 (C_2H_2)	CCH bend	(70)

Notes: (a) Carbonyl stretching region (saturated/unsaturated aldehydes/ketones with mono-/di-/tri-/tetra- substituted side chains)

Table S2. Calculated and Experimental Photoionization Cross-sections at 10.49 eV

Effective Charge (Z)	**Acetaldehyde (Mb)**	**Vinyl Alcohol (Mb)**	**Propanal (Mb)**	**(E)-1-Propenol (Mb)**	**(Z)-1-Propenol (Mb)**
0.0	7.8	11.5	2.9	5.1	9.6
0.2	12.0	14.6	8.1	8.3	13.2
0.4	16.6	13.5	10.7	9.3	12.0
0.6	16.8	12.2	10.9	9.7	9.6
0.8	14.6	10.9	9.8	9.9	8.8
1.0	12.3	10.7	9.1	9.8	9.6
Experimental Cross section	7.0 ± 2.0 (73) 7.4 ± 1.9 (67)	9.7 ± 2.4 (67)	10.0 ± 1.0 (73) 9.5 ± 1.9 (68)	Not Available	Not Available

Table S3. Derived Keto – Enol Branching Ratios Using Experimental and Theoretical Photoionization Cross Sections

Isomers	Raw Signal Ratios	Experimental Ratios*	Theoretical Ratios
Acetaldehyde : Vinyl alcohol	1.99 ± 0.14: 1	2.68 ± 1.02 : 1	2.15 ± 0.76 : 1
Propanal : (E)-1-propenol	3.65 ± 0.26: 1	3.20 ± 0.80 : 1	4.64 ± 2.84 : 1
Propanal : (Z)-1-propenol	3.65 ± 0.26: 1	4.23 ± 0.96 : 1	6.13 ± 3.71 : 1

*Ratios listed as "Experimental" include experimentally determined photoionization cross-section if available.

Table S4. Calculated vibrational frequencies with ωB97X-D/aug-cc-pVTZ and the vibrations observed for each molecule in the present experiments

Acetaldehyde (cm^{-1})		Vinyl Alcohol (cm^{-1})		Propanal (cm^{-1})		(E)-1-propenol (cm^{-1})	(Z)-1-propenol (cm^{-1})	(E)/(Z)-1-propenol (cm^{-1})
Computed (× 0.9566)	Observed Values	Computed (× 0.9566)	Observed Values	Computed (× 0.9566)	Observed Values*	Computed (× 0.9566)	Computed (× 0.9566)	Observed Values*
3018		3698		3007		3776	3771	
2977		3114	3239	2997		3037	3075	
2912		3055		2927		3015	3023	
2774		3012		2924		2975	3005	
1767	1728	1663	1635	2897		2953	2959	
1406		1422		2773		2898	2909	
1392	1427	1329		1763	1715	1712	1700	
1376		1292		1461		1448	1462	
1328	1350	1097	1130	1438		1426	1433	1435
1088	1120	1023		1404		1358	1396	
1085		947		1387		1328	1353	1340
863		866		1378		1294	1250	
727		722		1327		1175	1215	
498		493		1244		1120	1080	
97		452		1104		1076	1051	
				1089		1018	1022	
				984		936	933	
				875		898	914	
				832		808	744	
				665		522	662	
				625		312	459	
				266		299	276	
				243		236	227	
				120		205	99	

*Frequencies observed for the ^{18}O species of propanal or (E)/(Z)-1-propenol

Table S5. Comparison of theoretical and observational column densities for acetaldehyde and vinyl alcohol. The theoretical values represent peak results at around 10^6 yr.

Species Name	**Theoretical Result without Radiation Chemistry (molecules cm^{-2})**	**Theoretical Results with Radiation Chemistry (molecules cm^{-2})***	**Observational Value**
Acetaldehyde	5.6×10^{11}	$2.75 \pm 0.06 \times 10^{14}$	$2.2^{+1.1}_{-0.8} \times 10^{14}$ (38)
Vinyl Alcohol	1.7×10^{10}	$1.55 \pm 0.03 \times 10^{14}$	2.2×10^{14} (74)

* Note: Error ranges reflect uncertainties in experimental data from this work.

Table S6. Vinyl alcohol gas-phase processes and reactions added to the KIDA 2014 network. Rate coefficients for each process are calculated using the alpha, beta, and gamma values listed. The formulae used for rate coefficient calculations depend on the reaction type in the code (see footnotes for specific equations).

Cosmic-Ray Photon Induced Processes	α	β	γ	*Type*[‡]
$CH_2CHOH + CRP^{\dagger} \rightarrow HCO + CH_3$	7.280×10^{1}	0	0	2[a]
$CH_2CHOH + CRP \rightarrow CO + CH_4$)	7.280×10^{1}	0	0	2
$CH_2CHOH + CRP \rightarrow C_2H_4O^+ + e^-$	1.120×10^{3}	0	0	2

Photon Induced Processes	α (s^{-1})	β	γ	*Type*
$CH_2CHOH + Photon \rightarrow HCO + CH_3$	1.540×10^{-10}	0	1.520	3[b]
$CH_2CHOH + Photon \rightarrow CO + CH_4$	1.540×10^{-10}	0	1.520	3
$CH_2CHOH + Photon \rightarrow C_2H_4O^+ + e^-$	4.600×10^{-10}	0	2.280	3

Gas-Phase Reactions	α ($cm^3\ s^{-1}$)	β	γ (K)	*Type*
$CH_2CHOH + He^+ \rightarrow He + CH_3 + HCO^+$	1.400×10^{-9}	-0.5	0	4[c]
$CH_2CHOH + He^+ \rightarrow He + HCO + CH_3^+$	1.400×10^{-9}	-0.5	0	4
$CH_2CHOH + He^+ \rightarrow He + H_2 + H_2CCO^+$	1.400×10^{-9}	-0.5	0	4
$CH_2CHOH + He^+ \rightarrow He + H + CH_3CHO^+$	1.400×10^{-9}	-0.5	0	4
$CH_2CHOH + H_3^+ \rightarrow H_2 + CH_3CHOH^+$	7.440×10^{-9}	-0.5	0	4
$CH_2CHOH + C^+ \rightarrow CH + CH_3CO^+$	1.700×10^{-9}	-0.5	0	4
$CH_2CHOH + HCO^+ \rightarrow CO + CH_3CHOH^+$	3.000×10^{-9}	-0.5	0	4

$CH_2CHOH + H_3O^+ \rightarrow H_2O + CH_3CHOH^+$	3.430×10^{-9}	-0.5	0	4
$CH_2CHOH + H^+ \rightarrow H_2 + CH_3CO^+$	6.000×10^{-9}	-0.5	0	4
$CH_2CHOH + C \rightarrow C_2H_4 + CO$	3.000×10^{-10}	0.0	0	4
$CH_2CHOH + C^+ \rightarrow C_2H_4O^+ + C$	1.700×10^{-9}	-0.5	0	5[c]
$CH_2CHOH + H^+ \rightarrow C_2H_4O^+ + H$	6.000×10^{-9}	-0.5	0	5
$CH_2CHOH + CH_3^+ \rightarrow C_3H_6OH^+ +$ Photon	5.700×10^{-11}	-0.66	0	6[c]

---

‡ The type given is that used in the nautilus code for calculating the total rate. For more information, see documentation at https://git.framasoft.org/Wakelam/nautilus

† Cosmic-ray induced secondary UV photon

[a] Photodissociation and photoionization due to cosmic-rays with rate coefficients calculated using the formula $k = \alpha\zeta$, where ζ is the cosmic-ray ionization rate.

[b] External UV photodissociation and ionization with rate coefficients calculated using the formula $k(T) = \alpha e^{-\gamma Av}$, where Av is the visual extinction.

[c] Bimolecular gas-phase reactions using the modified Arrhenius formula, i.e. $k(T) = \alpha(T(K)/300)^{\beta}e^{-\gamma/T(K)}$

Table S7. Grain-surface processes and reactions for vinyl alcohol and acetaldehyde added to the Garrod et al. (2008) chemical network. Rate coefficients for non-diffusive processes, e.g. photodissociation, are calculated based on the alpha, beta, and gamma values listed below (see footnotes for specific formulae).

Thermal Desorption Processes	α	β	γ	*Type*[††]
$JCH_2CHOH \rightarrow CH_2CHOH$	1.000	0	0	15
$JCH_2CHOH \rightarrow CH_2CHOH$	1.000	0	0	16[a]

Cosmic-Ray Photon Induced Dissociation	α	β	γ	*Type*
$JCH_2CHOH + CRP^{\dagger} \rightarrow JCH_3 + JHCO$	5.250×10^2	0	0	17[b]
$JCH_2CHOH + CRP \rightarrow JCH_4 + JCO$	5.250×10^2	0	0	17
$JCH_2CHOH + CRP \rightarrow JCH_3 + JHCO$	3.730×10^2	0	0	18[b]
$JCH_2CHOH + CRP \rightarrow JH_2CCO + JH + JH$	3.730×10^2	0	0	18
$JCH_2CHOH + CRP \rightarrow JH_2CCO + JH_2$	3.730×10^2	0	0	18
$JCH_3CH_2OH + CRP \rightarrow JCH_2CHOH + JH_2$	6.850×10^2	0	0	18

UV Photon Induced Dissociation	α (s^{-1})	β	γ (K)	*Type*
$JCH_2CHOH + Photon \rightarrow JCH_3 + JHCO$	3.430×10^{-10}	0	1.520	19
$JCH_2CHOH + Photon \rightarrow JCH_4 + JCO$	3.430×10^{-10}	0	1.520	19
$JCH_3CH_2OH + Photon \rightarrow JCH_2CHOH + JH_2$	1.320×10^{-10}	0	2.350	20
$JCH_3COCH_3 + Photon \rightarrow JCH_2CHOH + JCH_2$	1.000×10^{-10}	0	2.500	20
$JCH_2CHOH + Photon \rightarrow JCH_3 + JHCO$	8.670×10^{-11}	0	2.280	20

UV Photon Induced Dissociation	*α* (s^{-1})	*β*	*γ* (K)	*Type*
$JCH_2CHOH + Photon \rightarrow JH_2CCO + JH + JH$	8.670×10^{-11}	0	2.280	20
$JCH_2CHOH + Photon \rightarrow JH_2CCO + JH_2$	8.670×10^{-11}	0	2.280	20

Cosmic-Ray Dissociation	*α* (s^{-1})	*β*	*γ* (K)	*Type*
$JH_2O \rightarrow JH^{st\ ‡} + JOH$	3.420×10^{-16}	0	0	21[c]
$JCH_4 \rightarrow JH^{st} + JCH_3$	3.420×10^{-16}	0	0	21

Photodesorption	*α* (s^{-1})	*β*	*γ* (K)	*Type*
$JCH_2CHOH + Photon \rightarrow CH_2CHOH$	1.000×10^{-3}	0	0	66
$JCH_2CHOH + CRP \rightarrow CH_2CHOH$	1.000×10^{-3}	0	0	67

Adsorption Processes	*α*	*β*	*γ*	*Type*
$CH_2CHOH \rightarrow JCH_2CHOH$	1.000	0	0	99

Grain-Surface Reactions	*α*[*]	*β*	*γ*	*Type*
$JCH_3 + JHCO \rightarrow CH_2CHOH$	0.373	0	0	14
$JCH_3 + JHCO \rightarrow JCH_2CHOH$	0.373	0	0	14
$JH + JCH_3CO \rightarrow CH_2CHOH$	0.373	0	0	14
$JH + JCH_3CO \rightarrow JCH_2CHOH$	0.373	0	0	14

$JH + JCH_2CHOH \rightarrow JCH_3OCH_2$	1.000	0	0	14
$JH + JCH_2CHOH \rightarrow CH_3OCH_2$	1.000	0	0	14
$JH^{st} + JCO \rightarrow JHCO^{st}$	1.000	0	0	14
$JH^{st} + JCH_3CO \rightarrow JCH_2CHOH$	0.373	0	0	14
$JH^{st} + JCH_3CO \rightarrow CH_2CHOH$	0.373	0	0	14
$JH^{st} + JCH_3CO \rightarrow JCH_3CHO$	0.627	0	0	14
$JH^{st} + JCH_3CO \rightarrow CH_3CHO$	0.627	0	0	14
$JC_2H_3 + JOH \rightarrow JCH_2CHOH$	0.373	0	0	14
$JC_2H_3 + JOH \rightarrow CH_2CHOH$	0.373	0	0	14
$JC_2H_3 + JOH \rightarrow JCH_3CHO$	0.627	0	0	14
$JC_2H_3 + JOH \rightarrow CH_3CHO$	0.627	0	0	14
$JHCO^{st} + JCH_3 \rightarrow JCH_2CHOH$	0.373	0	0	14
$JHCO^{st} + JCH_3 \rightarrow CH_2CHOH$	0.373	0	0	14
$JHCO^{st} + JCH_3 \rightarrow JCH_3CHO$	0.627	0	0	14
$JHCO^{st} + JCH_3 \rightarrow CH_3CHO$	0.627	0	0	14

[††] The specific formulæ used in nautilus are based on the reaction type. Note, species names beginning with "J" refer to those adsorbed onto grain-surfaces. For more information, see documentation at https://git.framasoft.org/Wakelam/nautilus.

[†] Cosmic-ray induced secondary UV photon

[‡] The "st" denotes a supra-thermal species

[*] Unitless branching ratios

[a] Desorption due to cosmic-ray grain heating

[b] Cosmic-ray induced UV photodissociation with rate coefficients calculated using the formula $k = \alpha\zeta$, where ζ is the cosmic-ray ionization rate.

[c] New reaction type for direct cosmic-ray dissociation

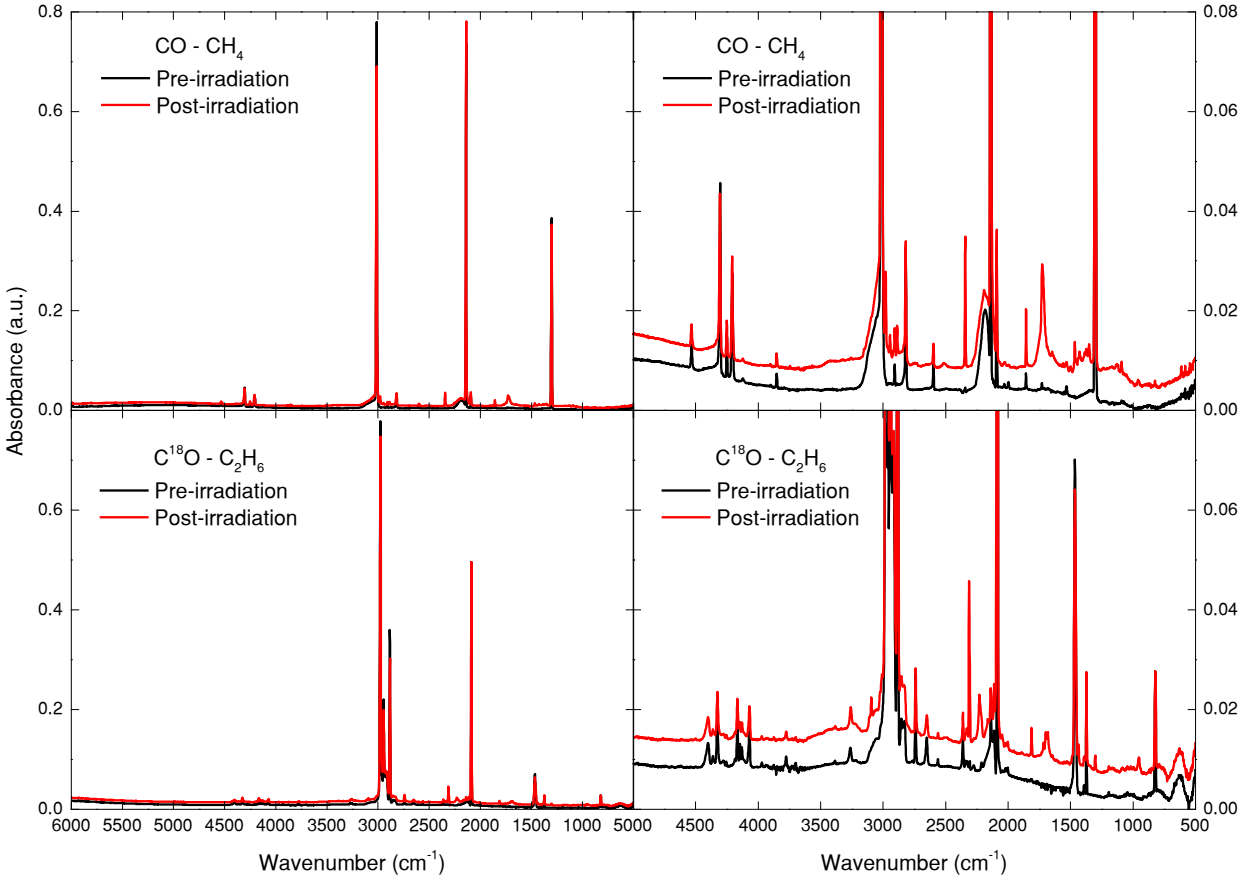

Figure S1. (Left) FTIR from 6000 – 500 cm^{-1} for (top) CO – CH_4 and (bottom) $C^{18}O$ – C_2H_6 before (black solid line) and after (red solid line) the irradiation period. (Right) FTIR from 5000 – 500 cm^{-1}. The baseline is offset between the pre- and post-irradiation spectra for clarity; the infrared assignments are compiled in Table S1.

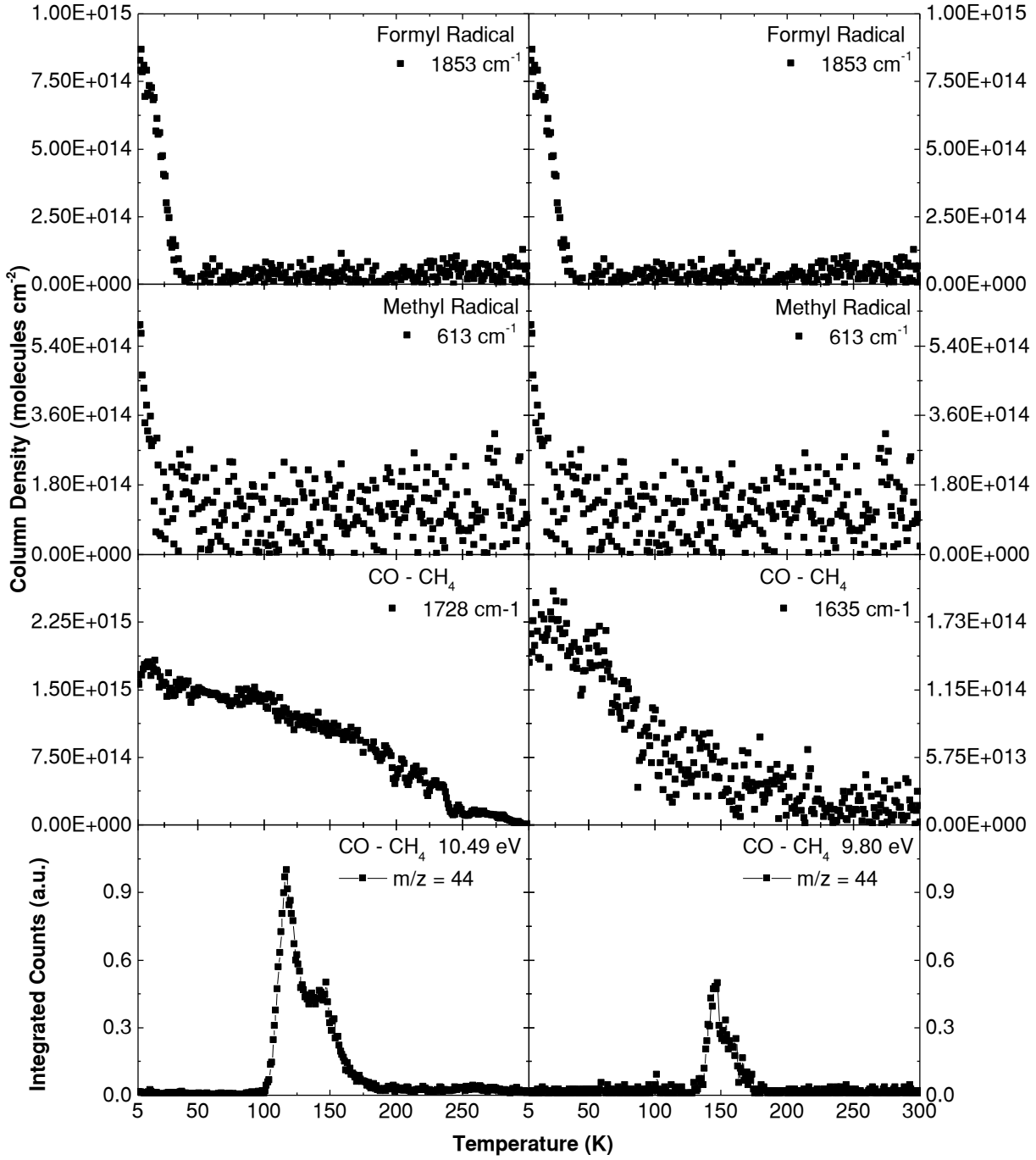

Figure S2. Integrated infrared area corresponding to molecules proposed to be a formation pathway for the keto – enol isomers. (Left, top-to-bottom) Integrated area of formyl radical, methyl radical, acetaldehyde, and the sublimation profile corresponding to acetaldehyde. This sublimation profile also contains the signal produced by vinyl alcohol. (Right, top-to-bottom) Integrated area of formyl radical, methyl radical, vinyl alcohol, and the sublimation profile corresponding only to vinyl alcohol.

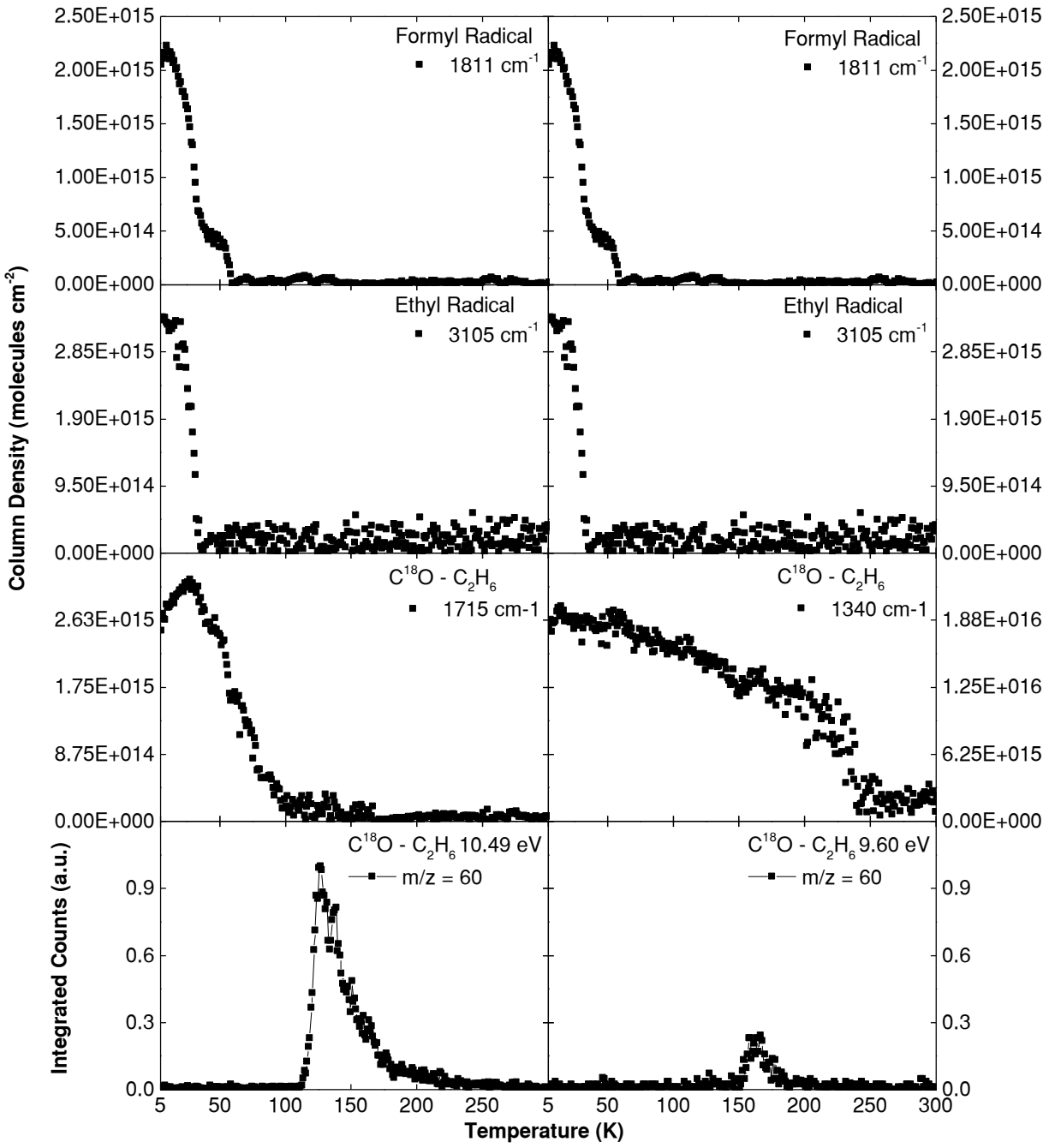

Figure S3. Integrated infrared area corresponding to molecules proposed to be a formation pathway for the keto – enol isomers discussed. (Left, top-to-bottom) Integrated area of formyl radical, ethyl radical, propanal, and the sublimation profile corresponding to propanal. However, this sublimation profile also contains the signal produced by (E)/(Z)-1-propenol. (Right, top-to-bottom) Integrated area of formyl radical, ethyl radical, (E)/(Z)-1-propenol, and the sublimation profile corresponding only to (E)/(Z)-1-propenol.

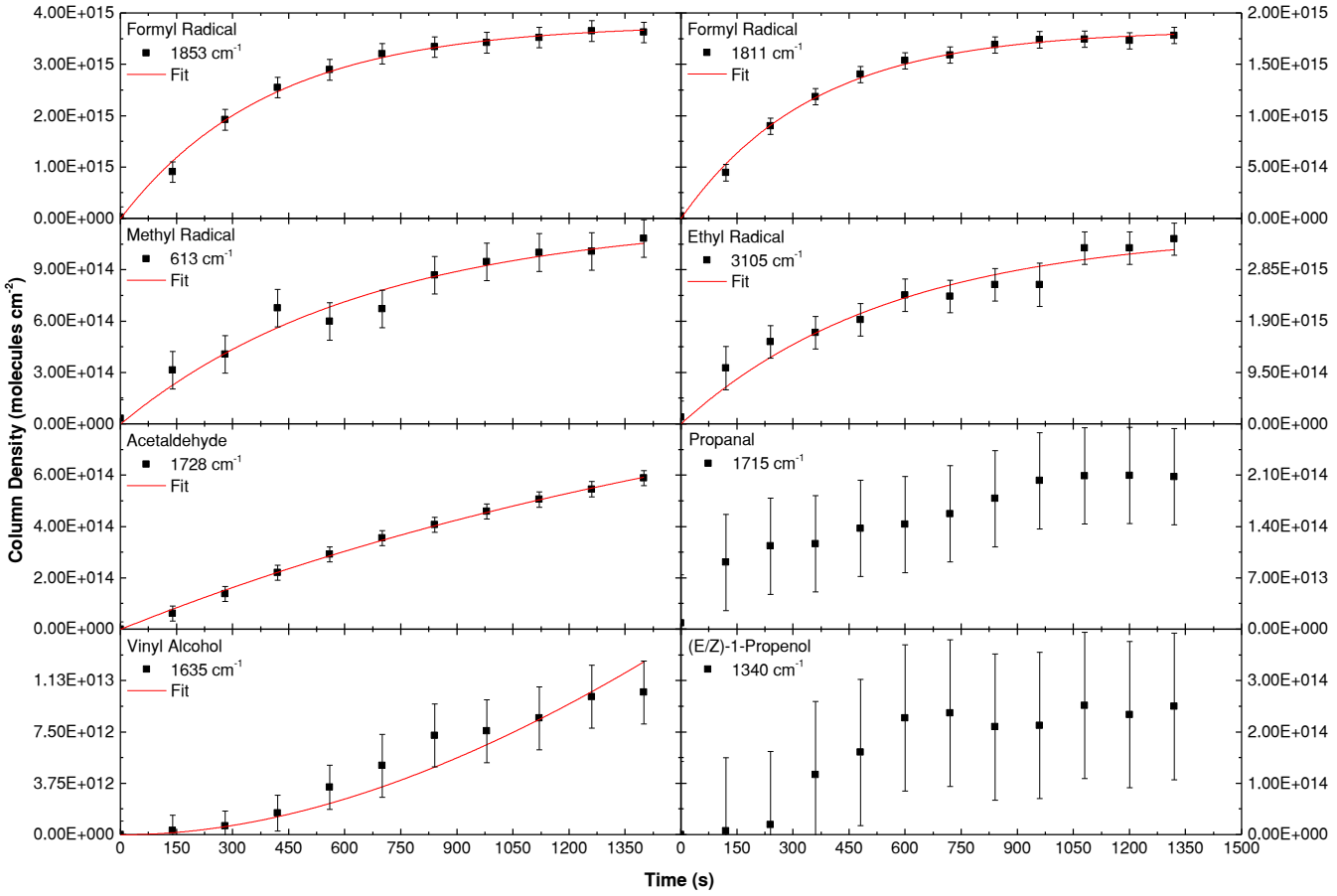

Figure S4. Integrated infrared area monitored for each ice. (Left) Temporal profiles of the formyl and methyl radical species produced in irradiated CO – CH_4 ice proposed to be utilized in the formation route of the keto – enol isomers as well as both isomers. (Right) Temporal profiles of the formyl and ethyl radical species produced in irradiated $C^{18}O$ – C_2H_6 ice proposed to be utilized in the formation route of the keto – enol isomers as well as both isomers. Note that due to large error associated with the data, infrared data for the propanal and (E)/(Z)-1-propenol isomers could not be uniquely fit.

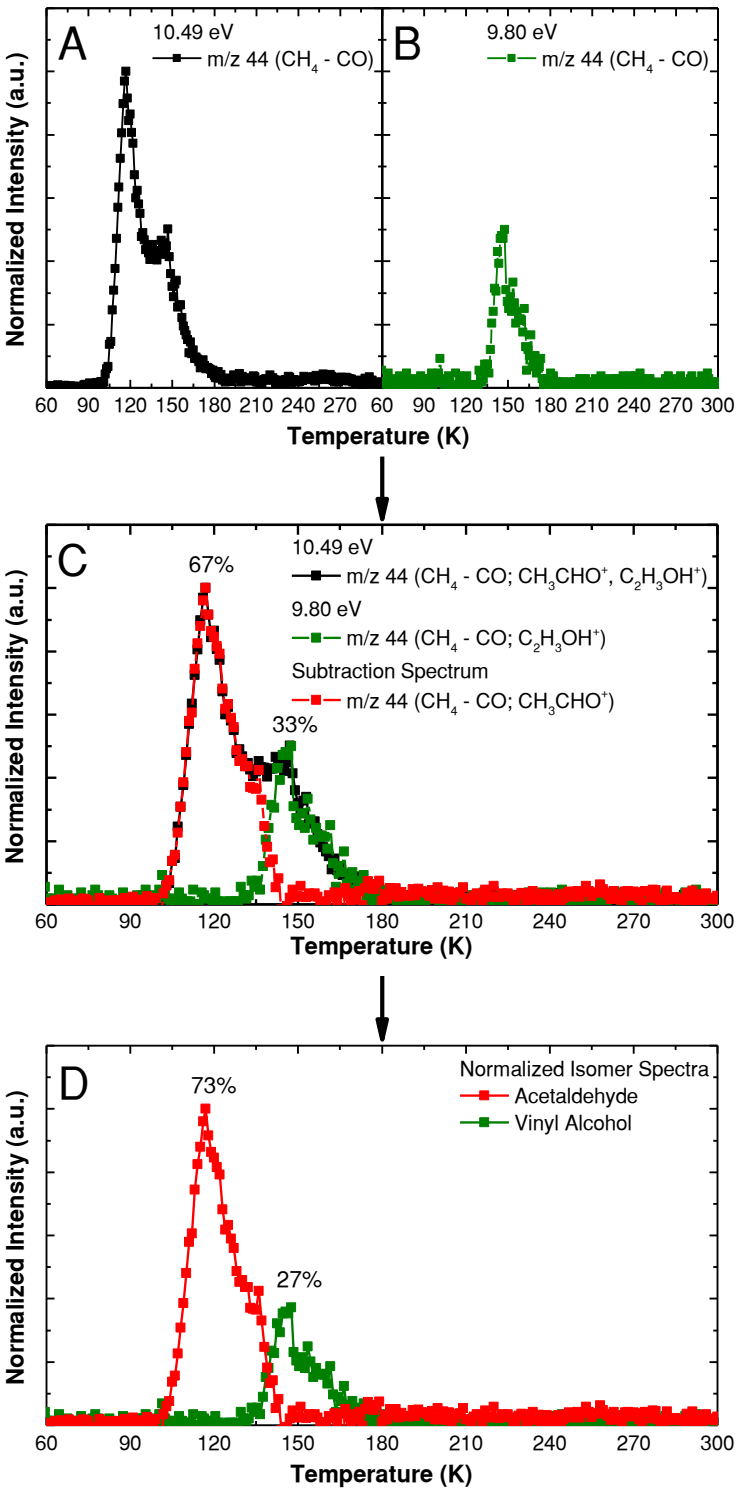

Figure S5. Flow diagram showing the procedure used to determine the relative ratios of the isomers in this experiment. A. The overlapping signal detected at 10.49 eV of both acetaldehyde and vinyl alcohol. B. The single signal of vinyl alcohol detected using tunable photoionization that was scaled to the signal observed at 10.49 eV. C. The scaled single isomer signal was subtracted from the overlapping signals allowing for the amount of each isomer contributing to the total signal to be determined (acetaldehyde-red, 67 %; vinyl alcohol-green 33 %). D. Isomer signals normalized by their respective photoionization cross-sections.